HARDENING OF Al–Si–Cu–Mg CAST ALLOYS: ROLE OF Ag AND Zn ADDITION

A. M. Samuel and F. H. Samuel
Université du Québec à Chicoutimi, Chicoutimi, QC, Canada

M. H. Abdelaziz
Département PEC, Université Française d'Égypte, Ville Shorouk, Caire, Egypt

H. W. Doty
Materials Engineering, General Motors Corporation, Pontiac, MI 48340, USA

Abstract

The present work was undertaken with the aim of studying the microstructural changes and intermetallic phases in Al-Si base 413.0 alloys as well as variations in tensile properties, including ultimate stress, yield strength and elongation at rupture, resulting from the addition of alloyed elements: strontium (Sr), magnesium (Mg), copper (Cu), silver (Ag), zinc (Zn) and nickel (Ni), to the base alloy 413.0, under different conditions of heat treatments, i.e., solutionizing and artificial aging (in the temperature range of 155 °C–240 °C). The results obtained in relation to microstructural observations and tensile tests reveal that the addition of alloying elements, in particular Mg, Cu, Ag, Ni, Zn and Sr, leads to an increase in the ultimate stress and yield strength values with a decrease in the strain levels of the base alloy 413.0, following hardening during artificial aging. Both Ag and Zn do not form specific phases during solidification at a slow rate of ∼ 0.8 °C/s but only segregate to the α-aluminum cell boundaries. Addition of 0.73% Ag improves the values of yield strength at all aging temperatures. Also, it enhances the alloy resistance to softening during aging in the temperature range 200–240 °C. Similar behavior was exhibited by the addition of 2.5% Zn.

Keywords: aluminum alloys, Ag, Zn, aging, tensile properties, solidification rate

Introduction

Artificial aging involves raising, for a sufficient period of time, the temperature of alloys in solid solution below the solvus curve of a given composition, in order to improve the mechanical properties. The solution, supersaturated with alloyed elements due to quenching, tends to return to the equilibrium state, passing through intermediate states where precipitates are formed in sequence consisting of agglomerates of atoms, in particular Guinier–Preston zones (GP zones), followed by metastable intermediate precipitates and finally by equilibrium precipitates. The return to equilibrium of the precipitates occurs more quickly as the aging temperature is high. The best mechanical properties of alloys are obtained when the solid solution contains GP zones and metastable precipitates of intermediate states.[1–3]

Heat-treatable Al-Mg-Si (-Cu) alloys constitute an important group of alloys whose mechanical properties can be increased by the precipitation of several metastable phases during heat treatments: aging, for example. Understanding and controlling precipitation during aging is therefore very important for obtaining optimal mechanical properties. The first stage in the precipitation sequence, the formation of the Guinier–Preston (GP) zones, is a complex process. According to previous studies, this stage could consist of three types of groups of atoms competing with each other: groups of atoms of silicon, magnesium and co-groups of atoms of magnesium and silicon.[4–8]

However, given the ultra-fine scale of atom groups, the details of the atom grouping process are not clearly established. According to recent studies, at this stage, copper would not have a significant effect on the chemical composition of the GP zones. Previous studies have shown that the predominant intermediate phase is the β" phase in the second stage of the precipitation sequence of Al-Mg-Si and Al-Mg-Si-Cu alloys. The β" phase has a needle shape and a monoclinic crystal structure. However, the copper content and the Mg / Si ratio could influence the crystal lattices parameter of the β" phase.

In fact, in the case of alloys with high copper content, the copper atoms have been shown to be incorporated into the lattice inside the needles of the β" precipitates, thus suggesting that the needle-shaped precipitates could be precursors of the metastable phase of the $Q-Al_5Mg_8Cu_2Si_6$ phase.[9]–alloy B) led to the formation of It is recognized that the precipitation process in Al-Mg-Si allIt is recognized that the prec

$$\alpha_{ssss} \rightarrow \text{GP Zones} \rightarrow \text{GP Zones} (\beta^{''}) \text{ needles}$$
$$\rightarrow \beta^{'} \text{ rodlike} \rightarrow \beta(\text{equilibrium platelets})$$
$$(\text{Coherent})(\text{Semi} - \text{Coherent})(\text{Non} - \text{Coherent})$$

where (ssss) constitutes the supersaturated solid solution and where the GP zone areas are anticipated in a spherical
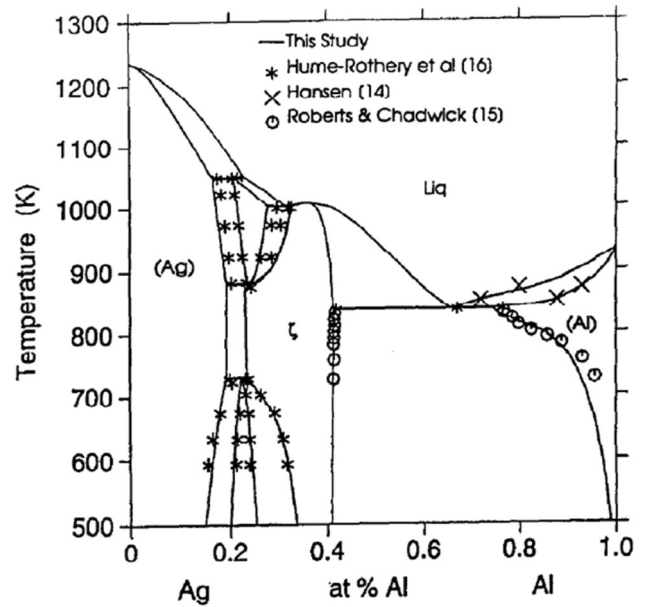

Figure 1. Phase diagram of Ag-Al: Comparison between the calculated phase diagram and the experimental data.[22]

shape and an uncertain structure. The term β" represents the precipitates in the form of a needle with a monoclinic structure having different values of the crystal lattice

Table 1. Chemical Composition (wt%) of the Alloys Used in the Present Study and Their Codes

Elements (%)	Alloys								
	413	A	B	C	D	E	F	G	H
Sr	<.0002	**0.0171**	**0.0193**	**0.0193**	**0.0264**	**0.0219**	**0.0229**	**0.0231**	**0.0240**
Mg	0.04	0.0751	**0.3890**	0.0732	**0.4490**	**0.4149**	**0.3260**	**0.3992**	**0.3820**
Cu	0.366	0.861	0.830	**2.747**	**2.284**	**2.573**	**2.592**	**2.786**	**2.638**
Ag	0.0016	0.0012	0.0013	0.0064	0.0013	**0.728**	0.0023	0.0038	0.0027
Zn	0.1128	0.2593	0.2646	0.2446	0.2512	0.2537	0.3133	**2.427**	**2.220**
Ni	0.10	0.0213	0.0219	0.0193	0.0230	0.0242	0.0198	0.0227	**0.845**
B	0.0034	0.0011	0.0032	0.0015	0.0028	0.0019	0.0017	0.0028	0.0024
Ti	0.0629	0.050	0.0564	0.0486	0.0593	0.0618	0.0497	0.0569	0.0601
Si	11.81	11.32	11.63	11.5	11.24	11.68	11.83	11.39	10.77
Fe	0.716	0.708	0.718	0.685	0.708	0.747	0.662	0.705	0.671
Mn	0.2804	0.2183	0.2159	0.2054	0.2076	0.2057	0.1911	0.2003	0.1897
Cr	0.0551	0.0183	0.0202	0.0175	0.0234	0.0267	0.0189	0.0193	0.0188
Pb	<0.0017	0.0085	0.0102	0.0089	0.0095	0.013	0.0124	0.0099	0.0084
Sn	<0.0024	<0.0024	<0.0024	0.0030	0.0031	0.0035	0.0227	0.0024	0.0027
Be	0.0024	0.0001	0.0001	0.0008	0.0073	0.0076	0.0007	0.0017	0.0013
Bi	<0.0025	0.00	<0.0025	<0.0025	<0.0025	<0.0025	0.00	<0.0025	<0.0025
Zr	.0057	0.0015	0.002	0.0015	0.0023	0.0025	0.0019	0.0019	0.0019
Co	< .0011	<.0011	<.0011	<.0011	<.0011	<.0011	.0086	<.0011	0.0014
V	0.0095	0.0076	0.008	0.0068	0.0077	0.0074	0.0082	0.0070	0.0.0069
Al	bal	bal	bal	bal	bal	bal	bal	bal	bal

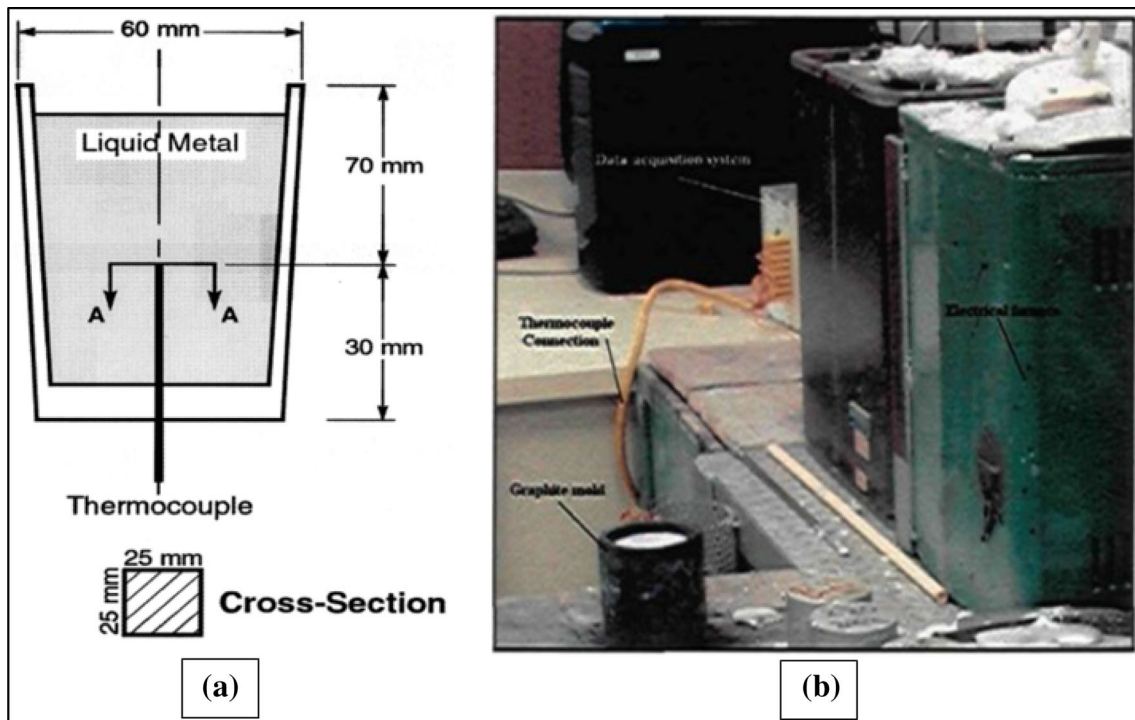Values in bold highlight the alloying additions in each alloy

Figure 2. (a) Schematic drawing showing the graphite mold and (b) set-up used for thermal analysis.
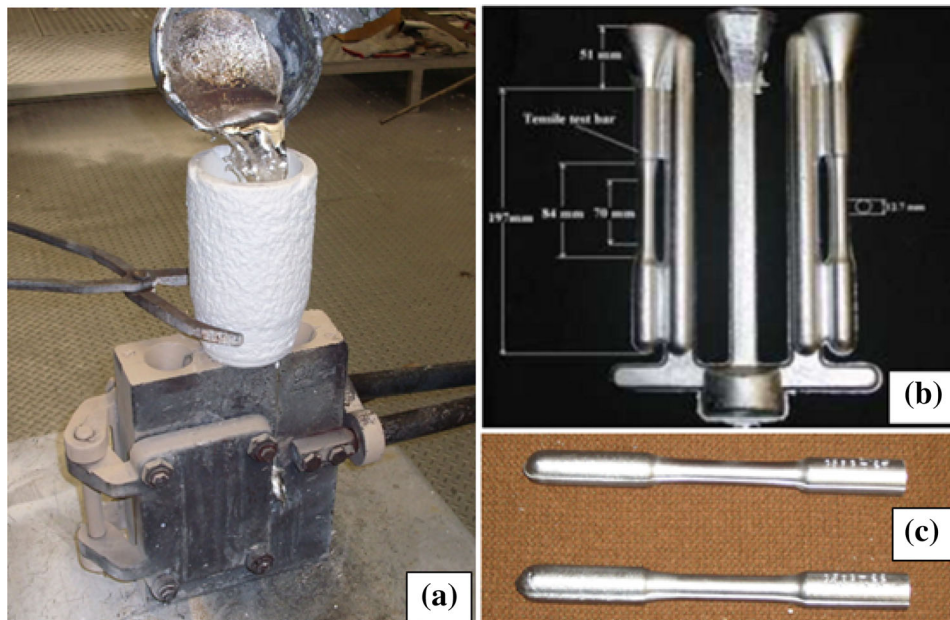

Figure 3. (a) Standard ASTM B-108 permanent mold and casting set-up used, (b) actual tensile test casting and (c) actual test bars sectioned from the casting.

parameters. The term β' represents the precipitates in the form of rods of circular section with a hexagonal crystal structure.[13] Finally, the β phase, which is the compound Mg_2Si, is normally formed of platelets with the crystal structure of CaF_2.

Thus, in addition to the above-mentioned precipitates normally present in Al-Mg-Si alloys, copper-containing precipitates such as θ-Al_2Cu and Q-$Al_5Mg_8Cu_2Si_6$ phases with their metastable phases may appear in the precipitation sequence of these alloys. While the θ phase has a

Table 2. Summary of the Reactions in Alloys 413, D, E and G

Alloy	Reaction (#)	Temperature (C)	Precipitation
413	1	573.6	Formation of the α-Al dendritic network
	2	568.8	Precipitation of the eutectic Al-Si
	3	525.0	End of solidification
D	1	565.6	Formation of the α-Al dendritic network
	2	561.6	Precipitation of the eutectic Al-Si
	3	537.0	Precipitation of the Mg_2Si phase
	4	520.3	Partial transformation of ß-Fe to π-Fe
	5	499.1	Precipitation of the Al_2Cu phase
	6	485.5	End of solidification
E	1	564.8	Formation of the α-Al dendritic network
	2	559.6	Precipitation of the eutectic Al-Si
	3	509.6	Precipitation of the Mg_2Si phase
	4	496.5	Precipitation of the Al_2Cu phase
	5	481.6	End of solidification
G	1	562.5	Formation of the α-Al dendritic network
	2	557.8	Precipitation of the eutectic Al-Si
	3	542.9	Partial transformation of Al_5FeSi to $Al_8Mg_3FeSi_6$
	4	492.2	Precipitation of the Al_2Cu phase
	5	466.5	Formation of the Q-$Al_5Mg_8Si_6Cu_2$ phase
	6	460.6	End of solidification

tetragonal centered structure, the composition of the proposed Q-phase would be hexagonal.[14–16] The precipitation sequence of Al-Si-Mg foundry alloys, the mechanical properties of which can be enhanced by aging, is represented by the following scheme:

GP zones → Intermediate precipitate
→ Mg_2Si equilibrium phase

Artificial aging is characterized by a behavior in which the mechanical strength and hardness of the alloys increase to a maximum and, subsequently, decrease when an overaging state is reached. The increase in strength properties is generally associated with a decrease in the percent strain and, as a consequence, a decrease in ductility.[17] The Al–Ag system is shown in Figure 1.[18,19] When the sample is quenched in the metastable fcc Al-rich miscibility gap, fcc-based GP zones form, whereas, when quenched from the high-temperature terminal fcc Al-rich solid solution phase, hcp precipitates form almost instantly.[20] Zarkevich and Johnson [19] verified the previously reported equilibrium ordered hcp Ag_2Al phase [21] and found a new equilibrium hcp AgAl phase. The AgAl ground state is predicted to be degenerate due to zero-energy domain boundaries and is expected to be relevant to precipitation.

The thermodynamic equilibrium state is determined by the relative Gibbs free energies of the phases present.[22] The Thermo-Calc package includes an optimization routine that fits the coefficients of the expression for the Gibbs free energy G*(T, x) for each phase (ph) as a function of temperature T and composition x to experimental thermochemical and phase diagram data for a system A-B, using the following equation:

$$G^{ph}(T,x) = x_A G_A^{ph}(T) + x_B G_B^{ph}(T)[x_A \text{In } x_A + x_B \text{In } x_B] + G^E$$

The experimental data can be compared with calculated values. Figure 1 shows the phase diagram calculated in this work compared with the experimentally determined phase diagram.[21] The agreement between the calculated and experimental results is within experimental error.

According to Demirtas et al.[23] and Li et al.,[24] the as-cast microstructure of the Al-8.1 wt pct Mg-2.6 wt pct Si alloy consists of the primary α-Al phase, Al-Mg_2Si eutectic phase and Al_3Fe phase. The AlMgZn intermetallic phase forms when Zn is added to the ternary alloy. When the Zn content is 1.01 wt pct, the s-$Mg_{32}(Al,Zn)_{49}$ phase forms in the microstructure, whereas the s-$Mg_{32}(Al,Zn)_{49}$ and g-$MgZn_2$ phases precipitate when the Zn content is 2.37 or 3.59 wt pct. The g-$MgZn_2$ phase is present when the Zn content is 4.62 wt pct. Saito et al.[25] concluded that Zn additions up to 0.1 wt% do not have a measurable influence on these properties and parameters. However, a slight increase in the material's hardness and a decrease in
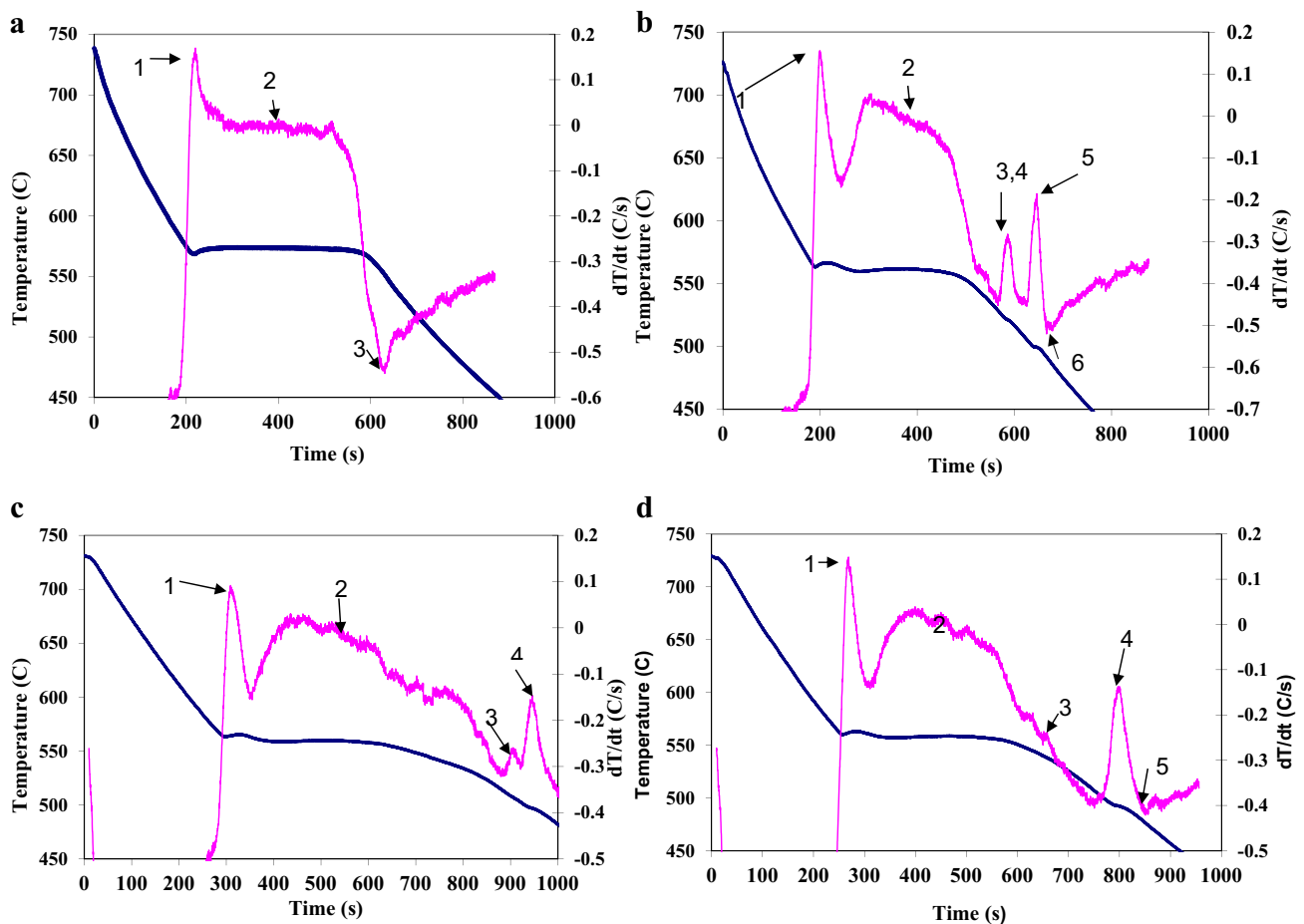
Figure 4. Solidification curves and their first derivatives: (a) base 413, (b) D alloy, (c) E alloy, (d) G alloy.

Table 3. Effect of Alloying Element on the Eutectic Temperature

Code	Eutectic Temperature. T_{eut} (°C)	Depression in $T_{eut.}$ ΔT (°C)
413	573.6	0.0
A	566.7	9.9
D	561.6	12.0
E	559.6	14.0
G	557.8	15.8

electrical conductivity have been detected at 1 wt% Zn. The higher hardness correlates with a quantified increase in precipitate number density and the presence of Zn in solid solution.

In a previous study,[26] the present authors focused on the formation of intermetallics during solidification of this series of alloys. The present work elaborates further on the analysis of the tensile properties in order to emphasize their hardening effect, in particular with the addition of Ag and Zn, elements which are present in Al–Si–Mg–Cu alloys widely used in high pressure diecasting. Through an extensive study of the precipitation behavior using electron microscopic techniques, the findings concretize the effects of these two additions on the precipitation strengthening in these alloys to explain the resulting tensile properties.

Experimental Procedure

The experimental procedure involved the preparation of 40 kg of molten metal in a SiC crucible heated by means of an electrical resistance furnace. Copper, Fe, Mn and Ni were added in required amounts to the molten metal, using Al-33% Cu, Al-25% Fe, Al-25% Mn and Al-20% Ni master alloys, respectively. Pure silver and zinc (99.9%) were added directly to the molten metal, while magnesium (99.9% pure) was added with a perforated graphite bell. Addition of the grain refiner (TiB_2) and modifier (Sr) was carried out using master alloys Al–5%Ti–1%B and Al–10% Sr, respectively. The modifier (Sr) was added to the molten metal just 5 min before the end of degassing. All the alloy melts were degassed for 30 min by injecting pure argon into the molten metal through a graphite impeller rotating at a speed of 135 rpm. Strontium was added to the melt 5 min before the end of degassing. The temperature of
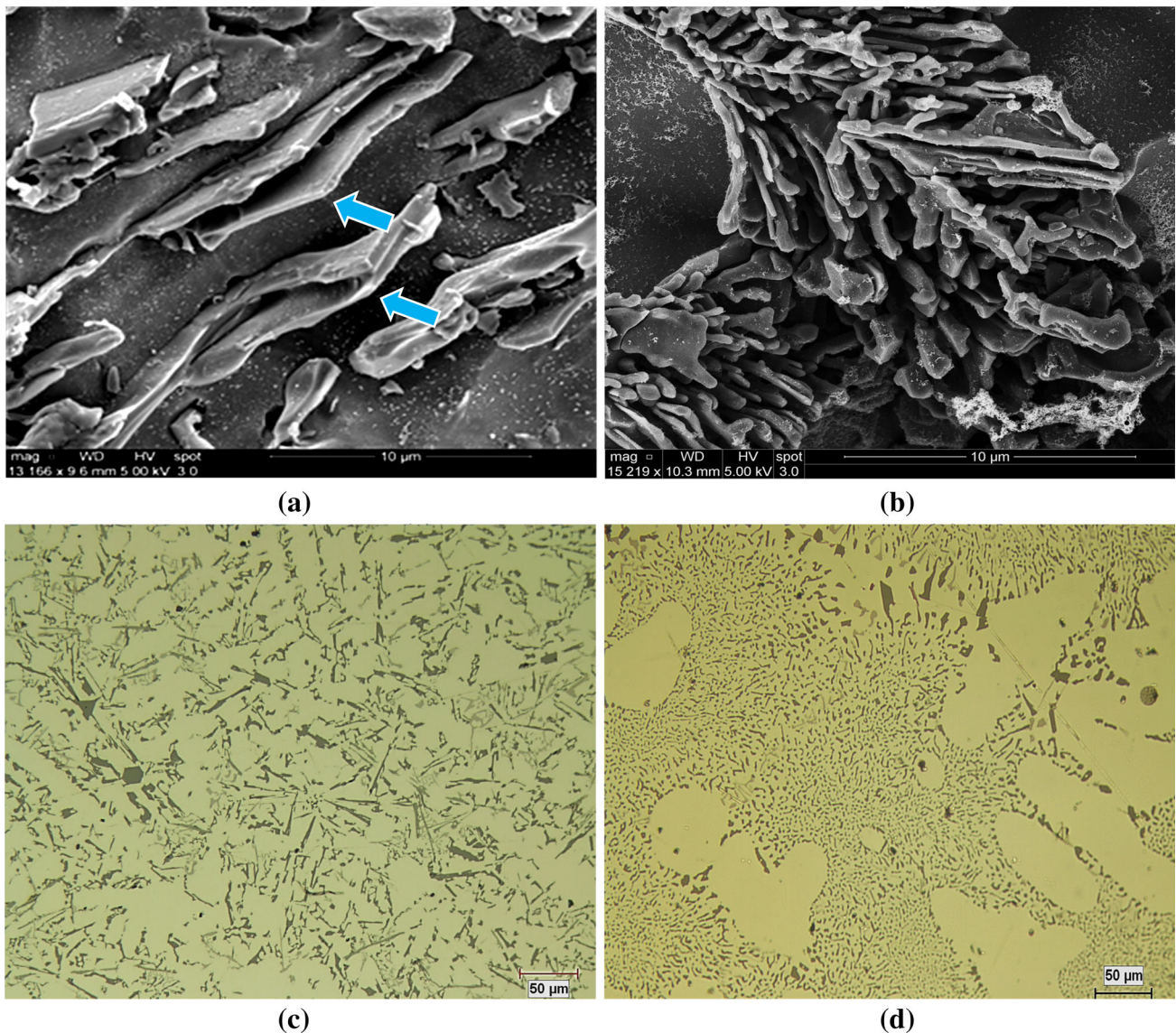
Figure 5. Microstructures of Si particles showing: (a) backscattered electron image of 413 alloy-0.8 °C/s, blue arrows point to sharp corners of Si platelets, (b) backscattered electron image of alloy A-0.8 °C/s, (c) 413 alloy-8 °C/ s, (d) alloy A-8 °C/s. Note the presence of α-Al in (d) due to depression in the eutectic temperature coupled with increase in the eutectic Si content.[38]

the molten metal was maintained at 720 ± 5 °C. For each composition of cast alloys, sampling for chemical analysis was carried out. The chemical compositions were analyzed by emissive spectroscopy and are listed in Table 1.

Thermal analysis consists of recording the evolution of the temperature of an alloy over time, from the liquid state to the solid state. It helps to identify the phases that form during the solidification process. The solidification curves describe the change in temperature over time, and their derived curve shows the stages of phase formation in these alloys. The thermal analysis was carried out for all the alloy castings by preheating them to 750 ± 5 °C. The liquid metal was poured into a graphite mold with a height of 80 mm and a diameter of 60 mm preheated to 600 °C,

and fitted with a high-sensitivity K-type thermocouple entering from below and positioned at the bottom of the mold cavity. The temperature-time data were collected by a high-speed data acquisition system (Strawberry Tree, acquisition speed: 1 reading per 0.2 second), connected to a computer equipped with curve plotting software. The part of the thermocouple included in the mold (except the end) is protected by a double-holed ceramic tube. The solidification time, t, was measured as the time interval between the onset of solidification and the precipitation of the Al_2Cu phase, as shown in Figure 2. The average solidification rate is approximately 0.8 °C/s.
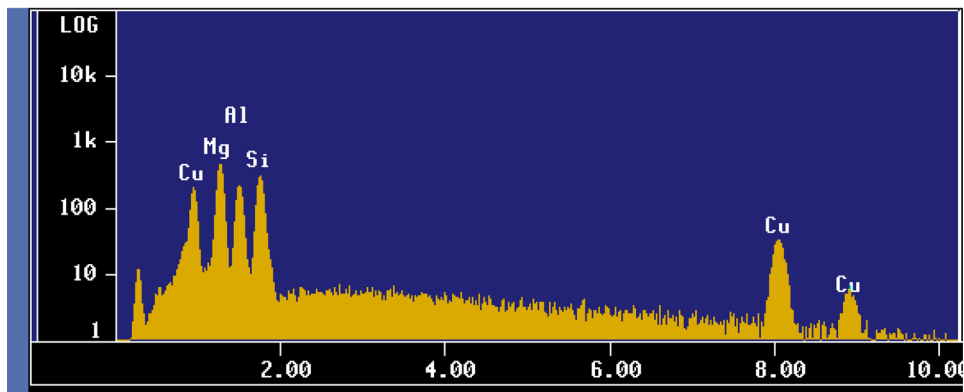
The various alloys were used to prepare castings from which test bars were obtained for tensile testing purposes.
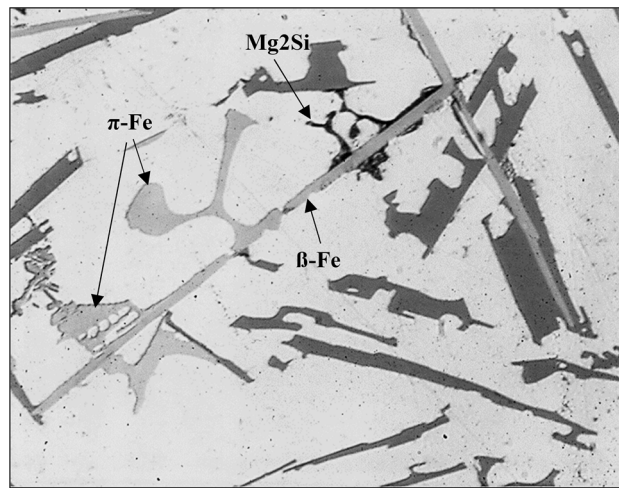
(a)
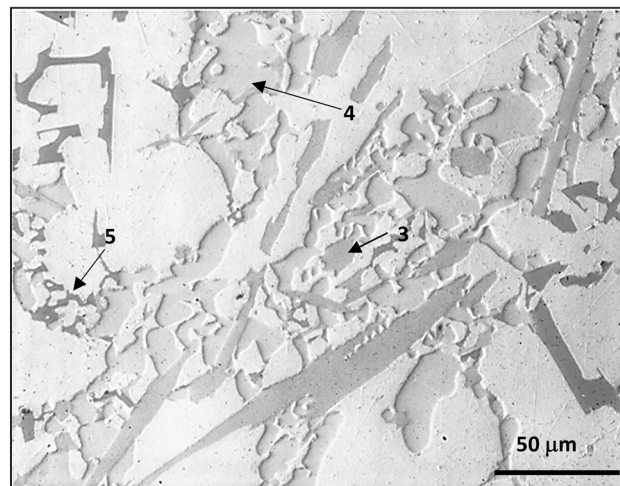
(b)

(c)

Figure 6. Optical micrographs of intermetallics containing Mg in (a) alloy B, (b) alloy D, showing (a) transformation of β-Al$_5$FeSi platelet to π-Al$_8$Mg$_3$FeSi$_6$ and precipitation of black script Mg$_2$Si on the untransformed part of the β-Al$_5$FeSi platelet; (b) precipitation of 3-Q-Al$_5$Mg$_8$Cu$_2$Si$_6$ phase intermixed in the Al-Al$_2$Cu eutectic regions; 4-massive Al$_2$Cu particles; five-ultra-fine Si particles indicating end of solidification (c) EDS spectrum corresponding to Q-phase in (b). Alloys were solidified at 0.8 °C/s.
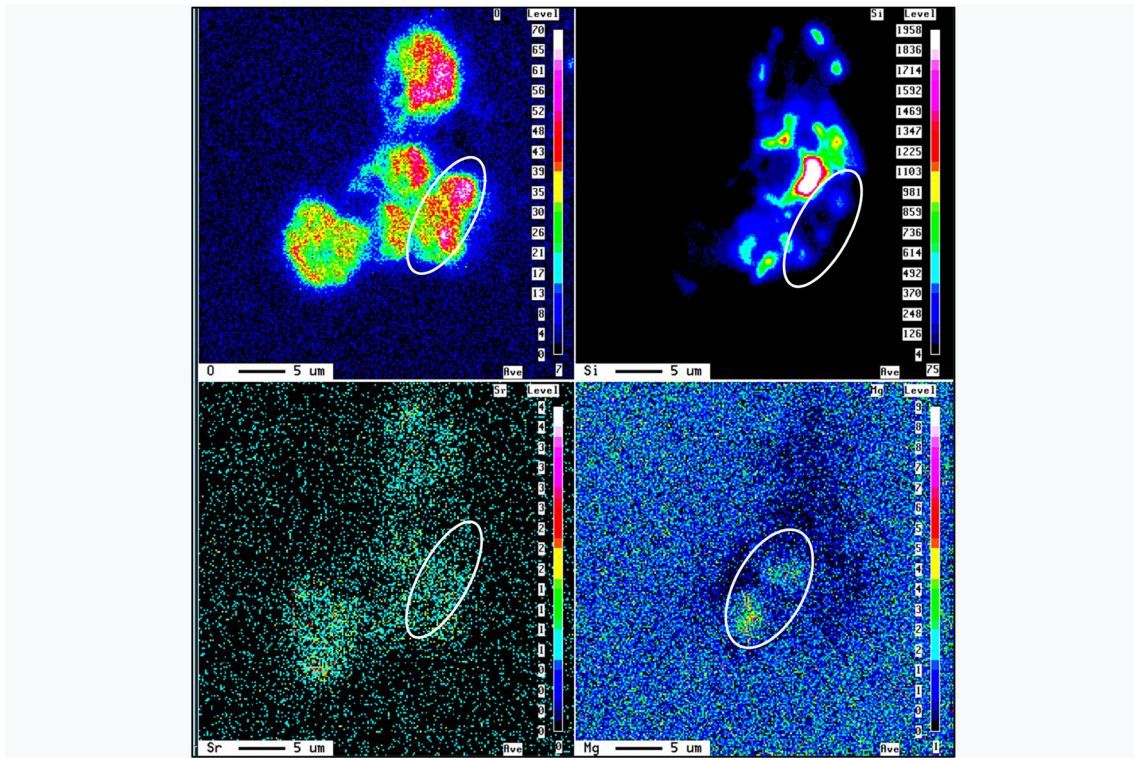
(a)
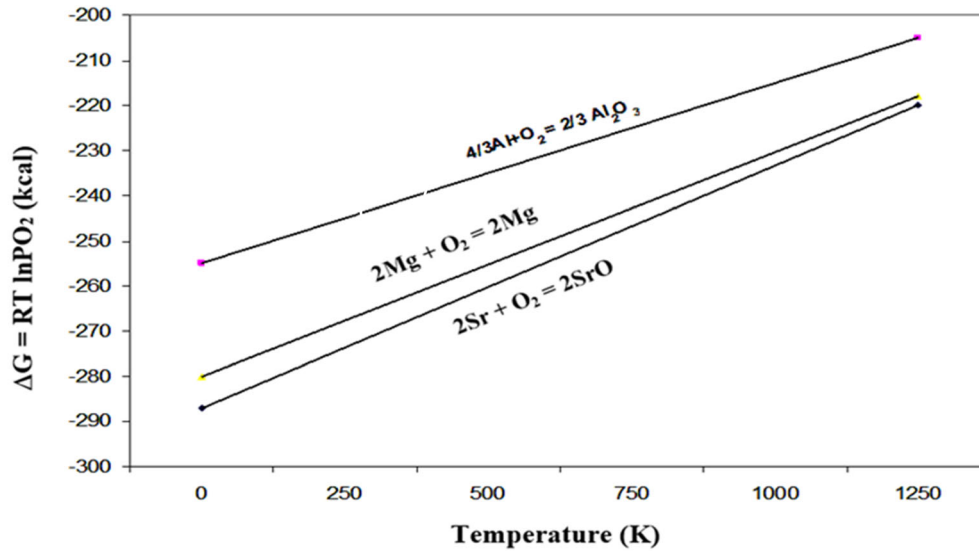
(b)

Figure 7. (a) X-ray colored maps of O, Sr and Mg interaction-white circles, (b) free energies of formation versus temperature for Al, Sr and Mg oxides.[39]

With this aim in mind, the degassed molten metal was carefully poured into an ASTM B-108 permanent mold preheated to 450 °C, to obtain castings for tensile testing. At the bottom of the pouring cup a ceramic foam filter (10ppi) was placed to prevent inclusions and oxide films from entering the mold. Each casting provided two test bars, each with a gauge length of 50 mm and a cross-sectional diameter of 12.8 mm, see Figure 3. The average solidification rate is about 8 °C/s.

The solution and aging heat treatments of the prepared tensile test bars were carried out in a forced-air Blue M electric furnace equipped with a programmable temperature controller, accurate to ± 2 °C. The quench delay was less than 10s. For each individual heat treatment, five test bars were used. Test bars corresponding to each alloy composition/heat treatment condition were pulled to fracture at room temperature at a strain rate of 4×10^{-4}/s using a Servo-hydraulic MTS Mechanical Testing machine. A
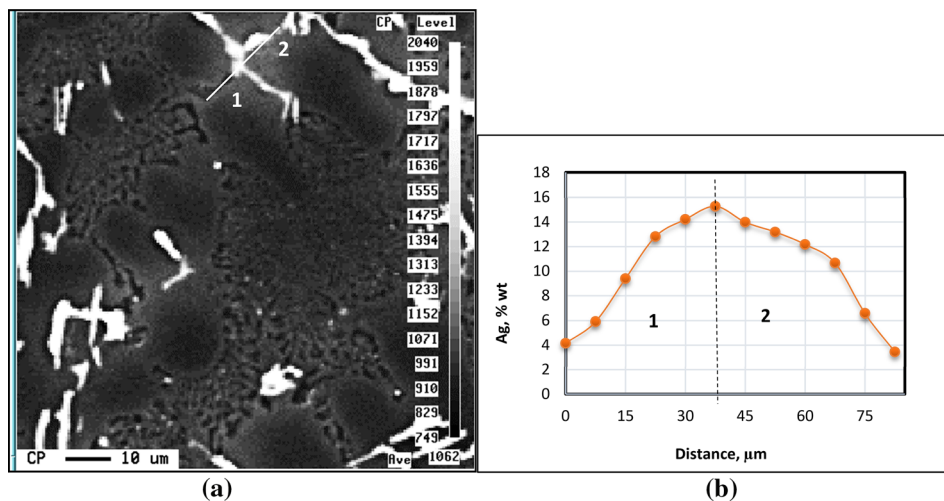
Figure 8. (a) Backscattered electron image of alloy E, (b) Ag distribution in alloy E along the white line.

strain gauge extensometer was attached to the test bar to measure percentage elongation as the load was applied. The yield strength (YS) was calculated according to the standard 0.2% offset strain, and the elongation to fracture was calculated as the percent elongation (%E_F) over the 50 mm gauge length. The ultimate tensile strength (UTS) was obtained from the data acquisition system of the MTS machine. The machine was calibrated each time before any testing was carried out. The average %E_F, YS and UTS values obtained from the five samples tested per alloy/condition were considered as the values representing that specified alloy/condition.

Samples for microstructural analysis were prepared from the castings obtained from the thermal analysis experiments and also from tensile-tested bars ~10 mm below the fracture surface. In the latter case, the samples were solution heat-treated (510°C/5h) followed by artificial aging for 5h at different temperatures in the range 155-240 °C. The microstructures of the polished sample surfaces were examined using an optical microscope linked to a Clemex image analysis system. A Hitachi SU-8000 field emission scanning electron microscope (FESEM), equipped with a standard secondary electron detector (SE), a backscatter electron detector (BSD) and energy-dispersive X-ray spectrometer (EDS) were used for examining the fracture surface. Line scans for Ag and Zn in E and G alloys, respectively, were obtained from the as-cast samples using an electron probe microanalyzer, equipped with EDX and WDS facilities.

Results and Discussion

Microstructure of the Solidified Alloys

Aluminum forms a variety of compounds with its allied elements. These intermetallic compounds are currently solid solutions which have a substantial capacity to dissolve other elements.[27] Although expressed by definite chemical formulas, these compounds exhibit a wide range of compositions[28] and precipitation temperatures.[29] In what follows, the intermetallic phases observed in our study will be discussed in accordance with their order of precipitation during solidification. Table 2 illustrates the different reactions which took place during the solidification of the base alloy as well as alloy D containing age hardening elements (Mg and Cu), and the E and G alloys. The data in Table 2 are taken from the experimental solidification curves shown in Figure 4. From Figures 4b and c, it is evident that the intensity of Mg_2Si is noticeably reduced when Ag is added to alloy D (*i.e.*, alloy G), suggesting a possible Ag–Mg reaction, whereas the same was further reduced with the addition of Zn (reaction #3).

Table 3 lists the eutectic temperature for the four alloys. Maximum depression in the eutectic temperature occurred when Sr was added to the base alloy (alloy A). As previously reported,[30] Mg addition as well results in increasing the reduction in the temperature of the Al-Si reaction. Apparently, the introduction of Ag or Zn has a noticeable effect on the Al-Si eutectic reaction.

Figure 5 shows the microstructures of the eutectic Si in base 413 and A alloys solidified at 0.8 °C/s and 8 °C/s. It is clearly evident that alloy A solidified at 8 °C/s (Figure 5(d)) produced finest particle size (approximately 4.03 μm^2 compared to 37.3 μm^2 in the case of base alloy 413 solidified at 0.8 °C/s) coupled with the disappearance of large Si platelets observed in Figure 5(a). The addition of Mg, up to ~ 0.4%, to the eutectic Al–11.7% Si alloy (i.e., alloy B) led to the formation of Mg_2Si and partial transformation of the β-Al_5FeSi phase into π-$Al_8Mg_3FeSi_6$.[31,32] An example of these two phases is shown in Figure 6(a). The Mg_2Si phase appears as black Chinese script particles. On the other hands, the π-$Al_8Mg_3FeSi_6$ phase, also
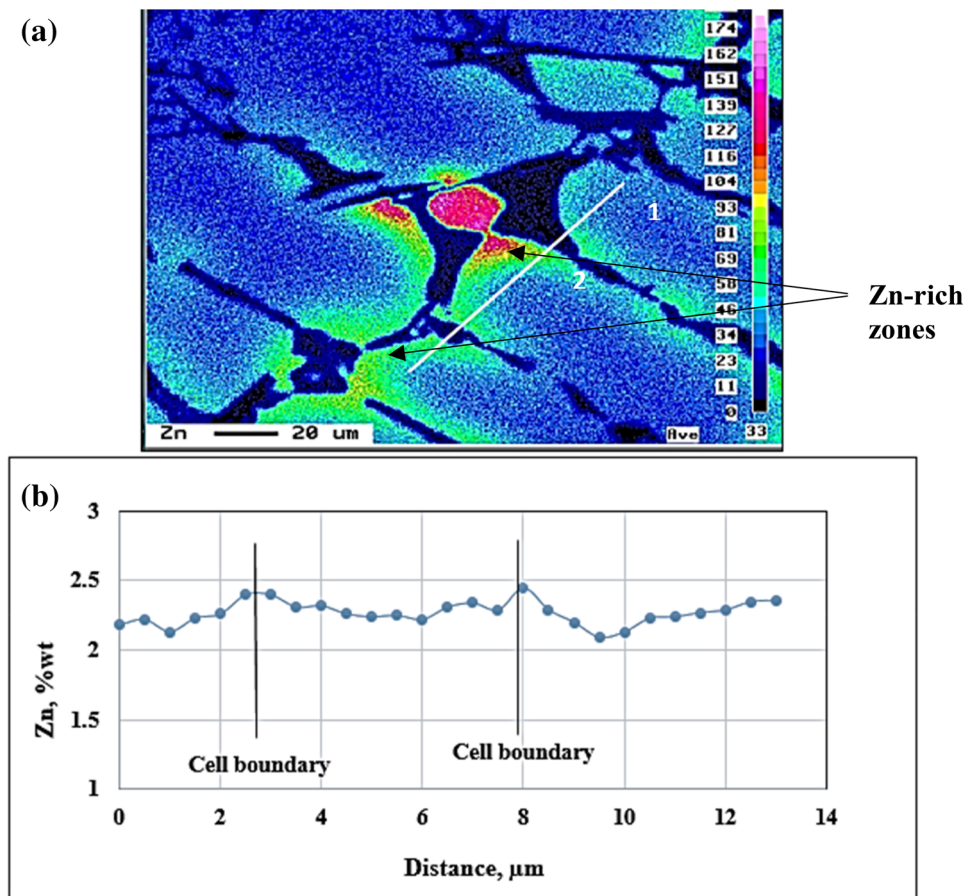
Figure 9. Zn distribution in alloy G solidified at the rate of 0.8° C/s: (a) X-ray image of Zn distribution, (b) Zn concentration along the white line in (a).

appearing in Chinese script form, is connected to the platelets of β-Al$_5$FeSi.

The Mg phase precipitates as gray Chinese script particles separately from the Al$_2$Cu phase, as shown in Figure 6(b), with a chemical composition corresponding to Q-Al$_5$Mg$_8$-Cu$_2$Si$_6$. When Cu is added to the Mg-containing alloy, in addition to Sr, i.e., alloy D, the Q-Al$_5$Mg$_8$Cu$_2$Si$_6$ phase precipitates as gray Chinese script particles intermixed in the regions of the Al$_2$Cu phase. Another point to be considered is the Sr-Mg interaction as displayed in Figure 7(a) due to their close free energies (Figure 7(b)). Obviously, such interaction would lead to reduction in the effectiveness of Mg as a hardening agent and Sr as a modifying element. In other words, when combined with Sr, Mg negates the effect of Sr modification to such an extent that a much higher level of Sr is required to achieve full modification of the eutectic Si structure. In the Sr-modified Mg-free alloy, the Al-Si eutectic is better modified than the one in the Mg-containing alloy modified using the same amount of Sr.[33]

Rosalie and Bourgeois[34] reported on Ag segregation to θ′ (Al$_2$Cu–Al interfaces in Al–Cu–Ag alloys. The precipitates nucleated on dislocation loops on which assemblies of γ′

(AlAg$_2$) enriched in silver appeared, prior to θ′ precipitation. The ground state of AgAl is predicted by Zarkevich and Johnson[21] to be degenerate due to zero-energy domain boundaries and is expected to be relevant to precipitation. Figure 8(a) depicts a backscattered electron image of alloy E (containing approximately 0.73% Ag and solidified at the rate of 0.8 °C/s). No explicit Ag-containing phase was detected in the interdendritic region. Instead, Ag was observed to be segregated at the boundaries of α-Al cells as shown by the scan presented in Figure 8(b). Similar observations were reported by Zaki et al.[35,36] in Al-Cu-Mg-Ag alloys. It should be noted that the distribution of Ag is wider than that reported for Zn.

Since the radius of the Zn atom (135 pm) is roughly equal to that of the Al atom (125 pm), Zn has high solubility in the Al matrix; the lattice distortion is low by adding Zn. The work of Yan et al.[37] on the effect of Zn addition on the microstructure and mechanical properties of an Al–0.66%Mg–0.87%Si alloy with 0.6% Zn reveals that with the precipitation of GP zones, β″ phase, GP(II) zones and η′ phase, the alloy displayed excellent mechanical properties. Saito et al.[25] showed that hardness of an Al-0.47%Mg-0.4%Si increases after aging at 185 °C if 1 wt % Zn is added to the alloy. The authors detected an increase
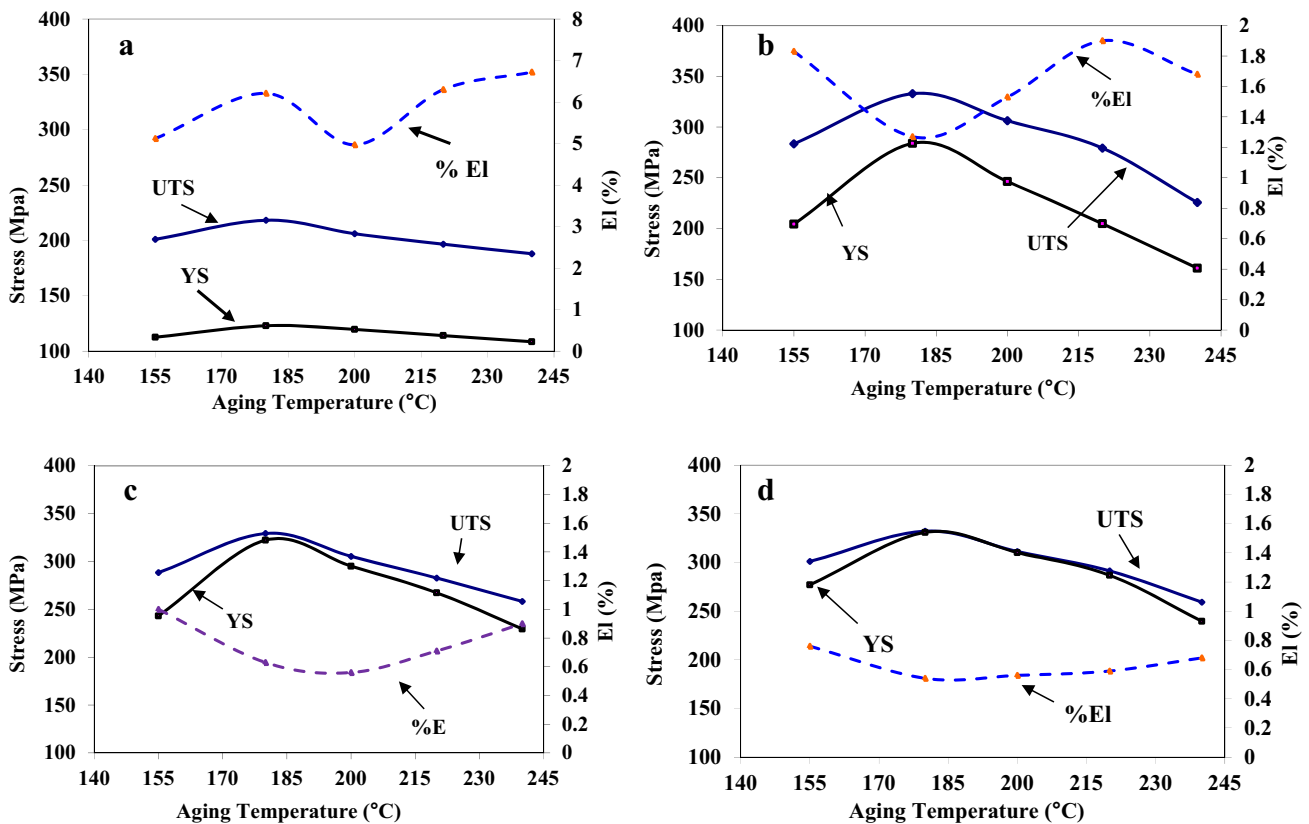
Figure 10. Tensile properties as a function of aging temperature for: (a) base alloy 413, (b) alloy D, (c) alloy E and (d) alloy G.

in the number density of needle-shaped precipitates from the Al–Mg–Si system, but no phases containing zinc. The Zn atoms segregated along grain boundaries, forming continuous films. Figure 9(a) depicts the Zn distribution in alloy G containing 2.4% Zn and solidified at the rate of 0.8 °C/s. The scan in Figure 9(b) reveals that Zn is mostly segregated at α-Al dendrite boundaries, similar to Ag. No precise phase could be detected using an FESEM microscope.

Tensile Properties

Figure 10 displays the values of the tensile properties of four alloys, i.e., the base alloy 413, as well as D, E and G alloys, following the application of different heat treatments of solution, quenching and artificial aging at five temperatures: 155 °C, 180 °C, 200 °C, 220 °C and 240 °C. It can be seen that the values of the ultimate tensile stress (UTS) and of the yield stress (YS) of alloys D, E and G (after artificial aging) are greater in all cases, than the corresponding values of UTS, YS and %El of the base alloy 413, reaching a maximum level at an aging temperature of 180 °C for the three alloys. Due to the absence of age hardening elements such as Mg or Cu in the base alloy, both UTS and YS were more-or-less horizontal with a slight increase at 180 °C (about 15 MPa) compared to an

increase of 115 MPa and 160 MPa in UTS and YS, respectively, in the case of alloy D aged similarly at 180 °C. Note that for alloys D and G, the deformation reached a minimum value at an aging temperature of 180 °C, and at 200 °C for base alloy 413.0 and alloy E.

Figure 10(c) reveals that addition of Ag to alloy D increased the alloy YS, reaching almost 320 MPa, a value close to the UTS reported for alloy E at 180 °C although it was difficult to detect precipitation of Ag-containing precipitates. However, addition of Ag seems to have no major effect on the alloy UTS level (330 MPa close to that in the case of alloy D at 180 °C). Another advantage of the addition of Ag appears in its contribution to the resistance to softening. For example, aging at 240 °C resulted in UTS values of 225 MPa and 260 MPa for alloys D and E, respectively. However, it should be noted that at 180 °C aging temperature, alloy D exhibited about 50 MPa difference in the values of UTS and YS compared to about 5 MPa in the case of alloy E. Addition of 2.5% Zn to alloy D, i.e., alloy G, resulted in UTS, YS, and %El values (see Figure 10(d)) close to those obtained for the addition of 0.73% Ag regardless of the aging condition.

The variations between the values of the tensile properties of alloys A to H (after aging treatment) and those of the base alloy 413 are shown in Figure 11, represented by ΔP
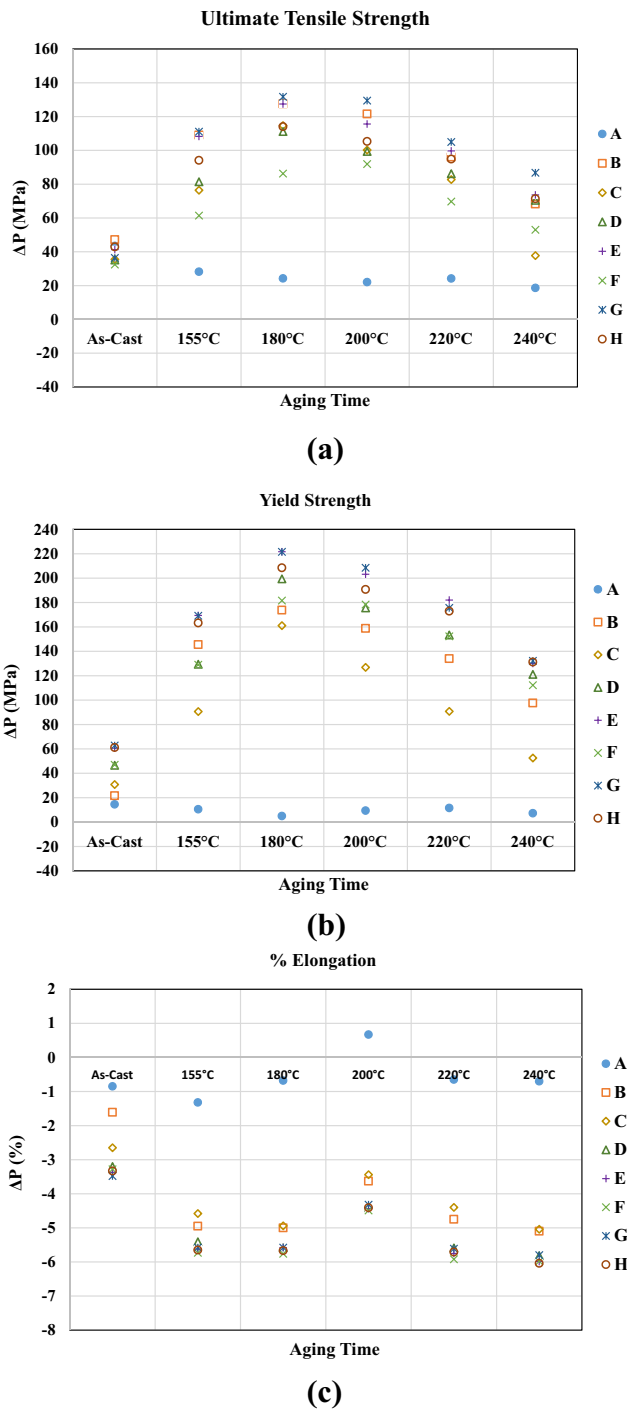
Ultimate Tensile Strength

(a)

Yield Strength

(b)

% Elongation

(c)

Figure 11. Variations in the tensile parameters as a function of alloying elements and aging temperature: (a) UTS, (b) YS and (c) %El.

values (P = Property) with the base line 0 representing the properties of the base alloy. The variations in the values of the UTS of the alloys (aged at 180 °C) reached a maximum increase of 132 MPa for the alloy G (alloy D + 2.4%Zn)

and alloy E (containing 0.73%Ag), then reduced gradually for the other alloys in the order D, B, C, H, F and A, the latter being the alloy with the lowest UTS: $\sim$ 24 MPa. The variations in the values of the YS for the alloys (aged at 180 °C) reached a maximum increase of 222 MPa for the alloys E and G, then reduced gradually for the other alloys in the order H, D, F, B, C and A, the latter showing the lowest yield strength increase of 5 MPa. As for the variations in the %El at failure of the alloys (at aging temperature of 180 °C), the alloy F showed the largest decrease in ∆P of 6%. Other alloys revealed decreasing ∆P values also, in the order H, E, G, D, B, C and A, the latter being the alloy having the lowest decrease in elongation at failure: 0. 68%. Figure 12 depicts an example of precipitation of Al_2Cu phase particles in the base alloy in the peak-aging condition, associated with a high dislocation density.

Fractography

Figure 13 shows the fracture behavior of some of the present alloys under different conditions. It should be mentioned here that all micrographs were obtained using secondary electron beam unless mentioned otherwise. Figure 13(a) corresponds to alloy 413 aged at 180 °C revealing the cracking of long unmodified Si particles (white arrows), whereas Figure 13(b) exhibits the fracture of α-$Al_{12}(Mn, Fe, Cr)_3Si_2$, as was confirmed by WDS analysis. Introduction of 170ppm Sr (alloy A) resulted in marked improvement in the fracture surface, Figure 13(c), showing complete dimple structure at 180 °C aging temperature. The higher magnification image in Figure 13(d) displays the perforation of an α-Fe script particle as inferred from the appearance of the dendrites through the α-Fe particle (arrowed). Samuel et al.[40,41] reported on the effect of Sr addition on the destabilization and fragmentation of α-Fe caused by Sr diffusion into Fe-containing intermetallics, which explains the perforation observed in Figure 13(d).

Figure 13(e) demonstrates the fracture of an Al_2Cu phase particle in alloy D in the as-cast condition (arrowed), whereas the backscattered electron image in Figure 13(f) reveals the dissolution of most of the Al_2Cu phase following solution heat treatment for 5h at 495 °C, with some traces at the bottom of deep dimples. Aging the same alloy at 180 °C/5h resulted in dense precipitation of fine Al_2Cu particles throughout as shown by the circled area in Figure 13(g). The enlarged micrograph shown in Figure 13(h) depicts this more clearly. The broken arrow in Figure 13(g) points to a particle of α-Fe. The presence of Ni in alloy H appeared in the form of platelets – marked X in Figure 13(i), mostly Al_9FeNi, as was confirmed by the
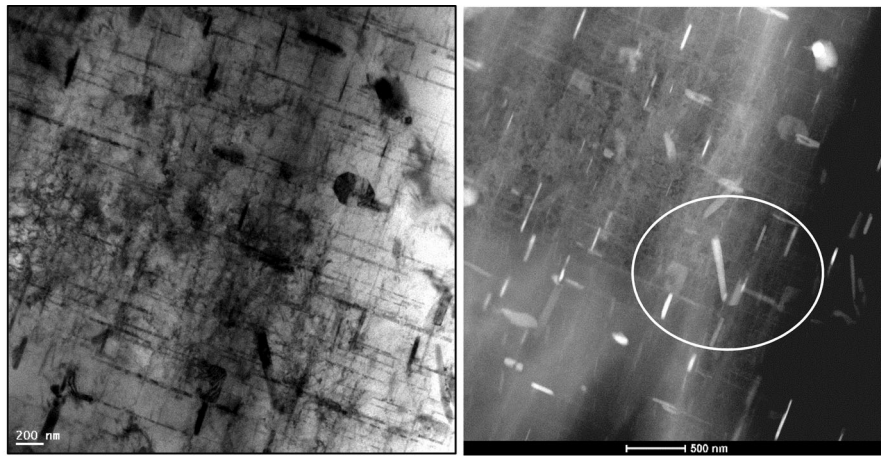
(a)

(b)
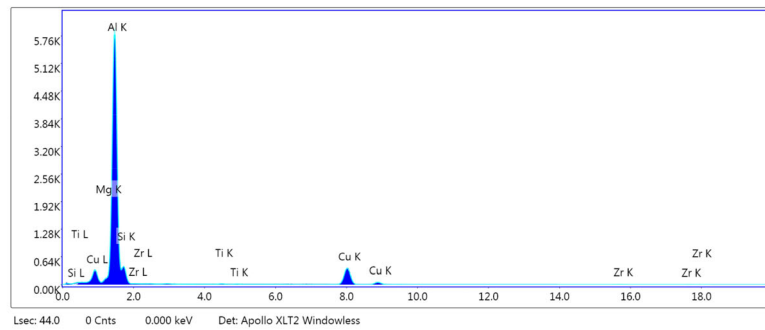
(c)

Chemical composition of the precipitates in the white circled area in (b).

Element	Weight %	Atomic %	Net Int.	Error %	K ratio	Z	A	F
MgK	1.80	2.03	38.70	9.28	0.0121	1.0176	0.6504	1.0102
AlK	72.16	73.16	2100.50	3.13	0.5268	0.9916	0.7340	1.0031
SiK	25.01	24.35	142.10	10.79	0.0313	1.0245	0.1221	1.0003
TiK	0.11	0.06	4.60	47.13	0.0003	0.9408	0.3032	1.0231
CuK	0.91	0.39	176.70	3.64	0.0084	0.9389	0.8669	1.1276
ZrK	0.01	0.00	1.80	66.62	0.0002	0.9175	1.1973	1.9699

(d)

Figure 12. *(a) Bright field electron image showing dense dislocations, (b) dark-field electron image revealing precipitation of ultra-fine Al$_2$Cu particles in the base alloy in the peak-aging condition; (c) EDS spectrum corresponding to the white circle in (b), (d) composition of the Al$_2$Cu precipitates.*

associated EDS spectrum of Figure 13(j) as well as WDS analysis.

Conclusions

From the data presented in this work, the following conclusions may be drawn:

1-Modification with 170ppm Sr coupled with a high solidification rate ($\sim$ 8 °C/s) is sufficient to produce a microstructure with fine eutectic Si particles ($\sim$ 4 μm^2) with no primary Si crystals.

2- During solidification at a slow rate ($\sim$0.8 °C/s), both Ag and Zn segregate toward the aluminum dendrite cells without formation of distinct phases.

3-The present results confirm observations from earlier studies on the destabilization of Fe-intermetallics in Sr-modified alloys, leading to their deterioration during heat treatment.

4-Sr has a strong affinity to react with Mg forming a complex compound. This reaction may be attributed to close values of their free energies.

5-Addition of (0.5%Mg +2.3% Cu) to Sr-modified 413.0 alloy (solidification rate ∼ 8 °C/s) increases both the UTS and YS values by about 87 MPa and 184 MPa, respectively, at the aging temperature of 180 °C.

6-Addition of either 0.73%Ag or 2.5%Zn to alloy D, further increases the UTS and YS values by ∼ 25 MPa and 30 MPa, respectively, at the same aging temperature.

7-The Ag and Zn additions also enhance the alloy resistance to softening during age hardening at high temperatures, i.e., 200–240 °C.
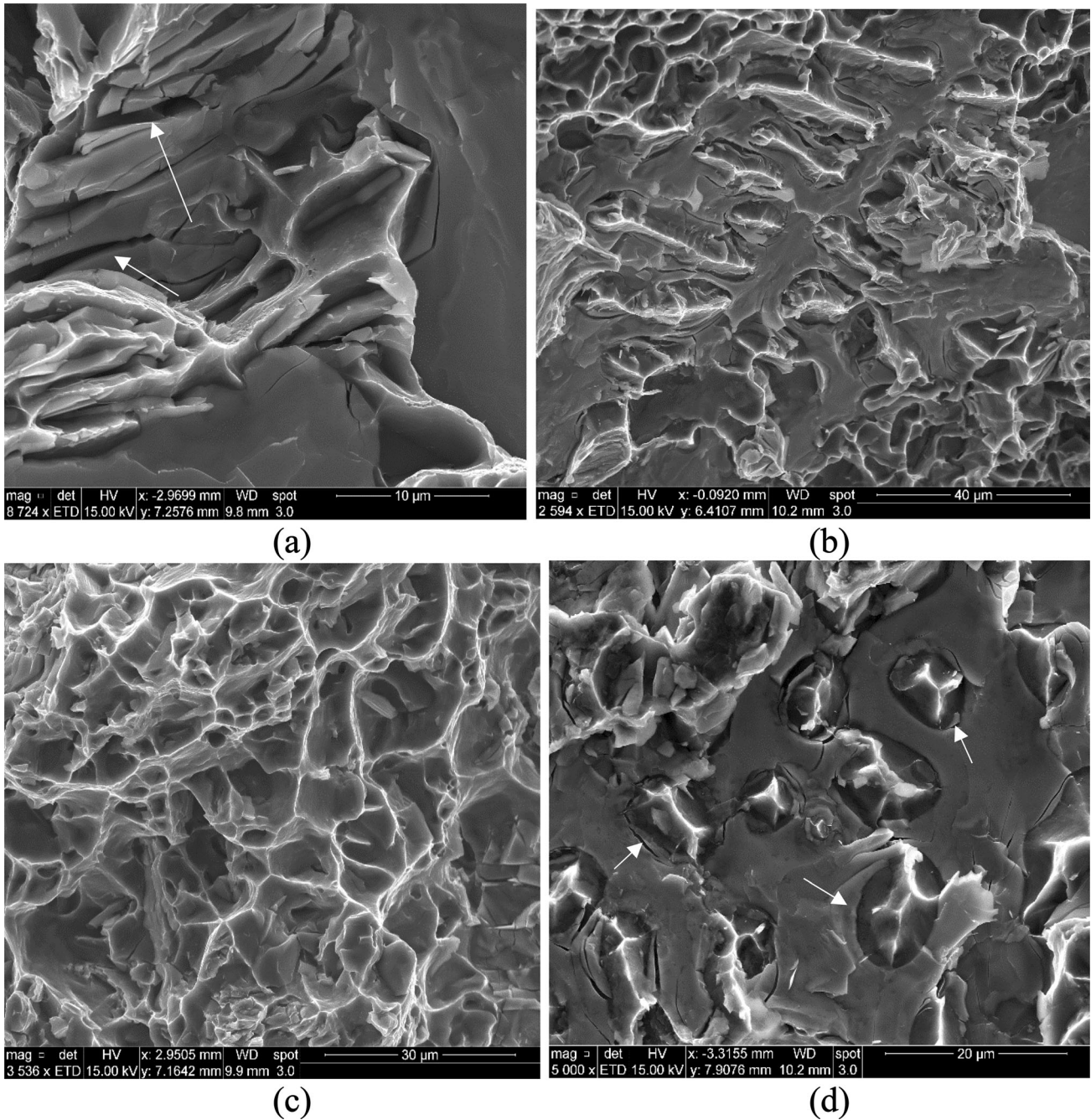

**Figure 13. Fracture behavior of the present alloys under different working conditions: (a) alloy 413 - aged at 180 °C/5h, (b) alloy 413 - same condition as (a), (c) alloy A - aged at 180 °C/5h, (d) alloy A - same condition as (c), (e) alloy D in the as-cast condition, (f) alloy D after solutionizing at 495 °C/5h, (g) alloy D aged at 180 °C/5h, (h) higher magnification image of (g), (i) alloy H aged at 180 °C/5h and (j) EDS spectrum corresponding to the area marked X in (h).**
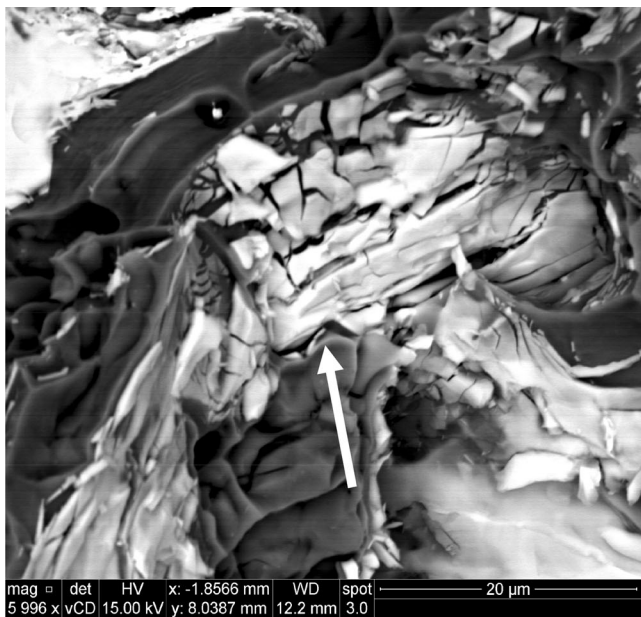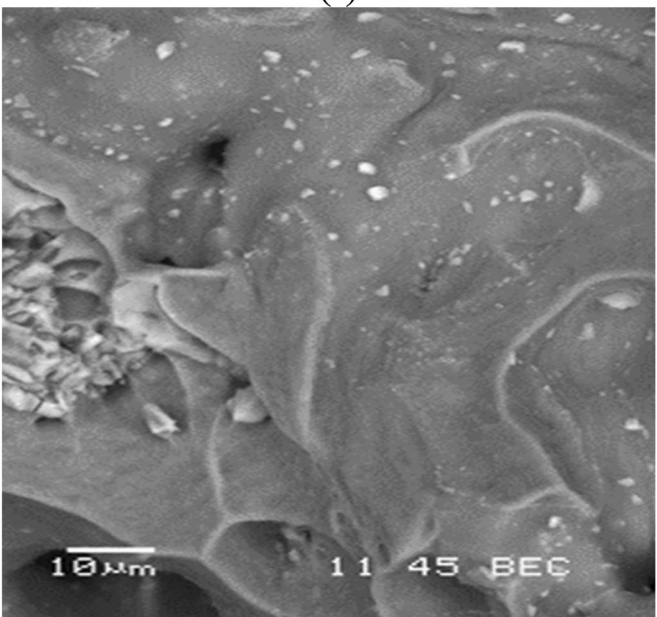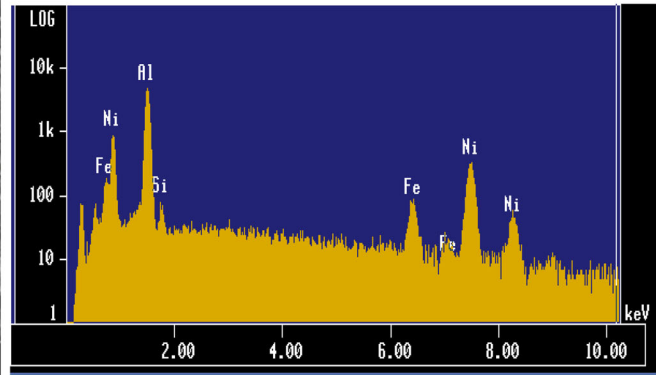
(e)
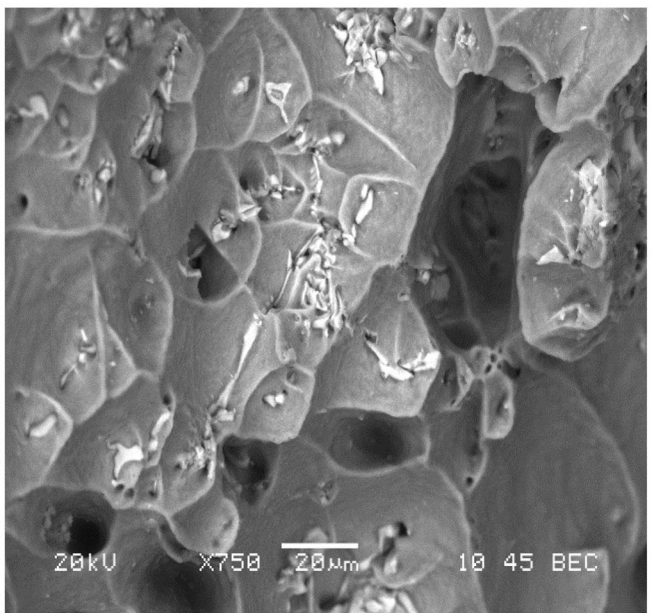
(f)
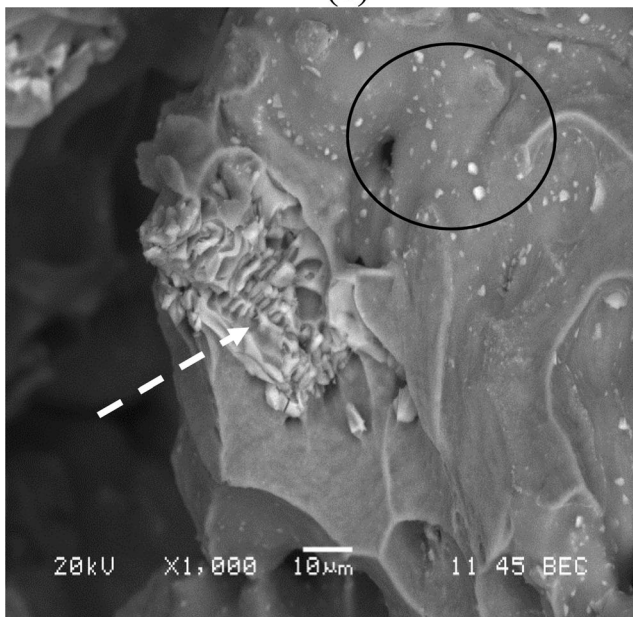
(g)

(h)

Figure 13. continued

(i)

(j)

Figure 13. *continued*

REFERENCES

1. M. Zeren, Effect of copper and silicon content on mechanical properties in Al–Cu–Si–Mg alloys. J. Mater. Process. Technol. **169**(2), 292–298 (2005)

2. E. Sjölander, S. Seifeddine, The heat treatment of Al–Si–Cu–Mg casting alloys. J. Mater. Process. Technol. **210**(10), 1249–1259 (2010)

3. C.H. Caceres, I.L. Svensson, J.A. Taylor, Strength-ductility behaviour of Al–Si–Cu–Mg casting alloys in T6 temper. Int. J. Cast Met. Res. **15**(5), 531–543 (2003)

4. P.S. Wang, S.L. Lee, J.C. Lin, M.T. John, Effects of solution temperature on mechanical properties of 319.0 aluminum casting alloys containing trace beryllium. J. Mater. Res. **15**(09), 2027–2035 (2000)

5. S.P. Ringer, K. Hono, Microstructural evolution and age hardening in aluminium alloys: atom probe field-ion microscopy and transmission electron microscopy studies. Mater. Charact. **44**(1), 101–131 (2000)

6. R. Molina, P. Amalberto, M. Rosso, Mechanical characterization of aluminium alloys for high temperature applications Part1: Al-Si-Cu alloys. Metall. Sci. Technol. **29**(1), 5–11 (2011)

7. H.R. Ammar, C. Moreau, A.M. Samuel, F.H. Samuel, H.W. Doty, Influences of alloying elements, solution treatment time and quenching media on quality indices of 413-type Al–Si casting alloys. Mater. Sci. Eng., A **489**(1), 426–438 (2008)

8. F.J. Tavitas-Medrano, J.E. Gruzleski, F.H. Samuel, S. Valtierra, H.W. Doty, Effect of Mg and Sr-modification on the mechanical properties of 319-type

aluminum cast alloys subjected to artificial aging. Mater. Sci. Eng. A **480**(1), 356–364 (2008)

9. D.G. Eskin, Decomposition of supersaturated solid solutions in Al–Cu–Mg–Si Alloys. J. Mater. Sci. **38**, 279–290 (2003)

10. S.K. Son, M. Takeda, M. Mitome, Y. Bando, T. Endo, Precipitation behaviour of an Al–Cu alloy during isothermal aging at low temperatures. Mater. Lett. **75**, 629–632 (2005)

11. S.P. Ringer, K. Hono, Microstructural evolution and age hardening in aluminum alloys: Atom Probe Field-Ion microscopy and transmission electron microscopy studies. Mater. Charact. **44**, 101–131 (2000)

12. C.R. Hutchinson, S.P. Ringer, Precipitation processes in Al–Cu–Mg alloys microalloyed with Si. Metall. Mater. Trans. A **31A**, 2721–2733 (2000)

13. S. Abis, M. Massazza, P. Mengucci, G. Tiontino, Early Ageing Mechanisms in a High-Copper AlCuMg Alloy. Scripta Mater. **45**, 685–691 (2001)

14. D. Emadi, L.V. Whiting, M. Sahoo, J.H. Sokolowski, P. Burke, M. Hart, Optimal heat treatment of A356.2 Alloy, in *Light Metals*. (The Minerals, Metals, and Materials Society, Warrendale, 2003), pp. 983–989

15. N.R. Andrade González, Aging Effects in 319-Type Alloys, PhD. Thesis, McGill University (2006).

16. D. Apelian, S. Shivkumar, G. Sigworth, Fundamental aspects of heat treatment of cast Al–Si–Mg Alloys. AFS Trans. **97**, 727–742 (1989)

17. F.H. Samuel, A.M. Samuel, H. Liu, Effect of Magnesium Content on the Aging Behaviour of Water-Chilled Al-Si-Cu-Mg-Fe-Mn (380) Alloy Castings. J. Mater. Sci. **30**, 1–10 (1995)

18. R.R. Hultgren, P.D. Desai, D.T. Hawkins, M. Gleiser, K.K. Kelley, *Selected Values of the Thermodynamic Properties of Binary Alloys* (American Society for Metals Park, Ohio, 1973).

19. A.J. McAlister, The Ag−Al (Silver-Aluminum) system. Bull. Alloy Phase Diagr. **8**, 526 (1987)

20. H. Okamoto (ed.), *Desk Handbook: Phase Diagrams for Binary Alloys* (ASM International, Materials Park, 2000)

21. N.A. Zarkevich, D.D. Johnson, Predicted hcp Ag-Al metastable phase diagram, equilibrium ground states, and precipitate structure. Phys. Rev. B, **67**(6), 1-7 (2003). id. 064104

22. S.S. Lim, P.L. Rossiter, J.E. Tibballs, Assessment of the Al–Ag binary phase diagram. Calphad **19**, 131–141 (1995)

23. M. Demirtas, G. Purcek, H. Yanar, Z.J. Zhang, Z.F. Zhang, Effect of chemical composition and grain size on RT superplasticity of Zn-Al alloys processed by ECAP. Lett. Mater. **5**(3), 328–334 (2015)

24. L. Li, S. Ji, Q. Zhu, Y. Wang, X. Dong, W. Yang, S. Midson, Y. Kang, Effect of Zn concentration on the microstructure and mechanical properties of Al-Mg-Si-Zn alloys processed by gravity die casting. Metall. Mater. Trans. A **49A**, 3247–3256 (2018)

25. T. Saitoa, S. Wenner, E. Osmundsen, C.D. Marioarab, S.J. Andersen, J. Røyset, W. Lefebvre, R. Holmestad, The effect of Zn on precipitation in Al–Mg–Si alloys. Phil. Mag. **94**(21), 2410–2425 (2014)

26. M.H. Abdelaziz, A.M. Samuel, H.W. Doty, S. Valtierra, F.H. Samuel, Effect of additives on the microstructure and tensile properties of Al–Si alloys. J. Mater. Technol. **8**, 2255–2268 (2019)

27. A. Mohamed and F. H. Samuel, A Review on the Heat Treatment of Al-Si-Cu/Mg Casting Alloys, in *Heat Treatment - Conventional and Novel Applications*, F. Czerwinski, Editor. 2012: InTech Open Access, Chapter 4, pp. 55-69. https://doi.org/10.5772/50282

28. W.D. Callister, *Fundamentals of Materials Science and Engineering: An Interactive E*, vol. 5 (Wiley, New York, 2001).

29. D. Eskin, Decomposition of supersaturated solid solutions in Al–Cu–Mg–Si alloys. J. Mater. Sci. **38**(2), 279–290 (2003)

30. A.M. Samuel, F.H. Samuel, Modification of iron intermetallics by magnesium and strontium in Al–Si alloys. Int. J. Cast Met. Res. **10**(3), 147–157 (1997)

31. E.A. Elsharkawi, M.H. Abdelaziz, H.W. Doty, S. Valtierra, F.H. Samuel, Effect of β-Al_5FeSi and π-$Al_8Mg_3FeSi_6$ phases on the impact toughness and fractography of Al–Si–Mg-based alloys. Int. J. Metalcast. **12**(1), 148–163 (2018). https://doi.org/10.1007/s40962-017-0153-8

32. E.A. Elsharkawi, A.M. Samuel, F.H. Samuel, E. Simielli and G.K. Sigworth, Influence of solutionizing time, modification, and cooling rate on the decomposition of Mg-containing iron intermetallic phase in 357 alloys. Transactions of the American Foundry Society, **120**, pp. 55-65; 116th Metalcasting Congress, April 17-20, 2012, Columbus, Ohio.

33. M.F. Ibrahim, E.M. Elgallad, S. Valtierra, H.W. Doty, F.H. Samuel, Metallurgical parameters controlling the eutectic silicon characteristics in Be-treated Al–Si–Mg alloys. Materials **9**, 78 (2016). https://doi.org/10.3390/ma9020078

34. J.M. Rosalie, L. Bourgeois, Silver segregation to θ' (Al_2Cu)–Al interfaces in Al–Cu–Ag alloys. Acta Mater. **60**, 6033–6041 (2012)

35. G.A. Zaki, A.M. Samuel, H.W. Doty, F.H. Samuel, Effect of metallrgical parameters on the performance of Al–2%Cu-based alloys. Int. J. Metalcast. **11**(3), 581–597 (2017). https://doi.org/10.1007/s40962-016-0113-8

36. G.A. Zaki, A.M. Samuel, H.W. Doty, F.H. Samuel, Effect of metallurgical parameters on the performance of Al–Cu based alloys. Int. J. Metall. Mater. Sci. Eng. **6**(1), 35–56 (2016)

37. Y. Yan, X. Zhang, F. Li, F. Li, H. Wang, H. Liu, B. Xiong, Effect of Zn addition on microstructure and mechanical properties of an Al–Mg–Si alloy. Mater. Int. **24**, 97–100 (2014)

38. G.F.V. Voort, J. Asensio-Lozano, The Al-Si phase diagram. Microsc. Microanal. **15**(2), 60–61 (2009). https://doi.org/10.1017/S1431927609092642

39. L. Liu, A.M. Samuel, F.H. Samuel, H.W. Doty, S. Valtierra, Influence of oxides on porosity formation in Sr-treated Al-Si casting alloys. J. Mater. Sci. **38**(6), 1255–1267 (2003)

40. A.M. Samuel, F.H. Samuel, Effect of Mg and Sr Addition on the Formation of Iron Based Intermetallics in Al-Si-Fe DC Alloys, in *International Symposium on Light Metals 1997 Métaux Légers as held at the 36th Annual Conference of Metallurgists of CIM.*, L.M. 1997, Editor. 1997: Sudbury, On., Canada. pp. 425-437

41. F.H. Samuel, G. Pucella, C. Villeneuve, A.M. Samuel, H.W. Doty, S. Valtierra, Microstructural observations on Fe-intermetallics in unmodified and Sr-modified Al-Si-Cu (A3801) die casting alloy. Int. J. Cast Metals Res. **12**(3), 197–210 (1999)

Publisher's Note Springer Nature remains neutral with regard to jurisdictional claims in published maps and institutional affiliations.